nature communications

Article

https://doi.org/10.1038/s41467-026-69193-7

Atypical protein kinase C activation drives intestinal glucose excretion in diabetes mellitus

Received: 16 May 2024

Accepted: 19 January 2026

Chan Woo Kang[1,15], Zhen-Yu Hong[2,15], Ju Hun Oh[1], Mohamed El-Agamy Farh[2,3], Eun Kyung Wang[1], Soohyun Lee[1], Un Ho Kang[2], Jung Ho Nam[1], Yang Jong Lee[1], Hyeju Shin[1], Ye Bin Kim[4], Hyeonuk Jeon[4,5], Jae Woong Jeong[6], Doyeon Kim[1], Jung Seung Kim[7], Seung Soo Hong[8], Jong-Pil Park[9], Hyo Je Cho[10], Sungsoon Fang[4,11], Hyongbum Henry Kim[4,12], Arthur Cho[13], Byung Kook Lim[14], Insuk Sohn[2] & Cheol Ryong Ku[1] ✉

Intestinal glucose excretion, defined as increased intestinal serum glucose uptake and secretion into the lumen, influences bariatric surgery-associated glycaemic control. Here, we investigate molecular mechanisms that activate intestinal glucose excretion. We evaluate altered transcriptomes in variable intestinal glucose excretion models and big data-based drug discovery systems. We show that protein kinase C (PKC) activation mimics transcriptome alterations observed during intestinal glucose excretion. Among PKC subfamilies, atypical PKC (aPKC) facilitates glucose transporter 1 (GLUT1)-mediated intestinal glucose excretion without inducing oncogenic proliferation. Intestinal aPKC activation via transposon expression vector induces serum glucose uptake into intestinal tissues and excretion into the lumen. Prostratin, a non-tumorigenic phorbol ester, activates aPKC and induces a similar effect on intestinal glucose excretion. We identify the prostratin and aPKC/GLUT1 signalling pathways as putative targets for treating diabetes, providing insights into the future development of antidiabetic and weight-loss drugs.

Type 2 diabetes is approaching epidemic proportions globally and poses major therapeutic challenges. Over three decades ago, Roux-en-Y gastric bypass (RYGB) was observed to improve glycaemic control in patients with type 2 diabetes[1,2], and subsequent multicentre trials have confirmed that gastric bypass is the most effective treatment for type 2 diabetes mellitus in patients with obesity[3,4]. However, the mechanisms underlying the rapid resolution of serum glucose levels after bariatric surgery remain unclear, and a

---

[1]Endocrinology, Institute of Endocrine Research, Department of Internal Medicine, Yonsei University College of Medicine, Seoul, Republic of Korea. [2]Arontier Corporation, Seoul, Republic of Korea. [3]AI-Bio Convergence Research Institute, Soongsil University, Seoul, Republic of Korea. [4]Graduate school of Medical Science, Brain Korea 21 PLUS Project for Medical Science, Yonsei University, Seoul, Republic of Korea. [5]Data Intelligence-driven Integrated Disease Research Center, Yonsei University College of Medicine, Seoul, Republic of Korea. [6]Institute for Immunology and Immunological Diseases, Yonsei University College of Medicine, Seoul, Republic of Korea. [7]NERIG Inc., Seoul, Republic of Korea. [8]Division of Hepatobiliary and Pancreatic Surgery, Department of Surgery, Yonsei University College of Medicine, Seoul, Republic of Korea. [9]Department of Forensic Medicine, Yonsei University College of Medicine, Seoul, Republic of Korea. [10]Department of Biochemistry, Chungbuk National University, Cheongju, Republic of Korea. [11]Department of Biomedical Sciences, Gangnam Severance Hospital, Yonsei University College of Medicine, Seoul, Republic of Korea. [12]Department of Pharmacology, Yonsei University College of Medicine, Seoul, Republic of Korea. [13]Department of Nuclear Medicine, Yonsei University College of Medicine, Seoul, Republic of Korea. [14]Neurobiology Section, Division of Biological Sciences, University of California, San Diego, La Jolla, CA, USA. [15]These authors contributed equally: Chan Woo Kang, Zhen-Yu Hong. ✉e-mail: CR079@yuhs.ac

pharmacological agent that can mimic this effect has not yet been identified.

We previously identified amphiregulin (*Areg*), an epidermal growth factor receptor (EGFR) ligand, as being crucial for increasing glycolysis and intestinal glucose excretion in hypertrophic intestinal enterocytes after RYGB[5–7]. We further demonstrated a critical link between intestinal glucose excretion and enhanced glucose homeostasis using ^{14}C-labeled glucose tracer to directly assess intestinal glucose excretion, suggesting that *Areg*/EGFR/glucose transporter 1 (GLUT1) signal transduction may play a vital role in type 2 diabetes[5]. Accumulating evidence has demonstrated altered functional expression of glucose-related transporters, including sodium-glucose co-transporter and GLUT1, after surgery or diabetes induction in mice[8–11]. Saeidi et al. used fluorodeoxyglucose (FDG) imaging to demonstrate the intestine's role as a major glucose depository[11]. We further validated this finding by demonstrating that *Areg* induction causes serum glucose excretion into the intestinal lumen via GLUT1, which is activated without bowel hypertrophy. However, the mechanism has not been elucidated thus far.

Advances in in silico analysis have greatly improved the efficiency of drug discovery[12,13]. In silico analysis allows not only the analysis of the effectiveness of developed or developing drugs using big data but also the discovery of novel therapeutic targets with minimal side effects and maximal efficacy[14].

Arontier.co (Seoul, Republic of Korea) developed the REMEDY approach based on Connectivity Map (CMap)[15], a database containing differential gene expression profiles obtained by exposing various cell types to diverse perturbagens, including small molecules. This database contains over 1,000,000 gene expression profiles subjected to over 20,000 small molecules via the introduction of L1000 assay technology[16]. L1000-based CMap has been broadly utilised for drug repurposing and has identified small molecules that induce gene expression profiles and cancel or mimic the differential gene expression induced by diseases[17,18]. This approach functions as phenotypic screening, which is a counter approach to target-based drug discovery; that is, the small molecules that induce the target phenotypes (e.g., gene expression) in cellular or animal models are first identified, and their underlying mechanisms are subsequently investigated.

Accordingly, we implemented this approach to identify the most effective drugs/targets that could mimic RYGB-induced intestinal glucose excretion in normal non-excretory intestines (thereby changing the gene expression profile of normal rat intestinal tissue into that of glucose-excretory intestinal tissue). We applied transcriptomes from five different pairwise comparisons of intestinal glucose excretion and non-glucose excretion tissue/cells to REMEDY to screen and identify potential drug/target candidates that could mimic glucose-excretory intestines. We further validated the identified candidates by conducting various biological experiments. Finally, we aimed to identify the downstream molecules that mediate the function of the identified target as an effective activator of intestinal glucose excretion.

Results

CMap-based drug/target identification

Consistent with our previous findings[5], compared with sham operation, RYGB significantly upregulated the expression of EGFR ligands, including *Areg*, epiregulin, and heparin-binding EGF-like growth factor (HB-EGF), in the common limb (CL) (Supplementary Fig. 1a). The upregulation of intestinal GLUT1 after RYGB has been well documented as the major factor in the enhanced glucose homeostasis caused by RYGB (Supplementary Fig. 1b)[5]. To investigate their functional role, we examined the effects of various EGFR ligands on GLUT1 expression and glucose uptake in intestinal cell lines. Among the tested EGFR ligands, HB-EGF induced the most significant GLUT1 overexpression and glucose uptake (Supplementary Fig. 1c, d). Glucose homeostasis was improved in HB-EGF-injected mice compared to that in vehicle-injected mice (Supplementary Fig. 1e). Thus, we further compared the differentially expressed genes (DEGs) in HB-EGF-treated normal intestinal cell lines and post-RYGB intestinal samples.

To identify the most effective drugs/targets that can mimic the intestinal glucose excretion effect of RYGB in intestinal tissues, DEGs from five pairwise comparisons of glucose-excretory and non-excretory tissues/cells were investigated (Fig. 1B) using the transcriptome-based drug discovery platform REMEDY (Fig. 1A). Firstly, DEGs collected from five sets of glucose-excretory and glucose non-excretory tissues/cells were taken as query signatures (list of genes whose expression is correlated with a biological state of interest) (Fig. 1B). The highest similarity was detected using a pattern-matching algorithm (KS-modified algorithm), and the best candidate drugs with a mechanism of action (MoA) that could induce similar gene expression changes as the query were screened out among signatures in the Library of Integrated Network-Based Cellular Signatures (LINCS) database. As a result, the protein kinase C (PKC) activator scored the highest in four sets, except the set of RYGB AL vs. sham JEJU (Fig. 1C–G). Comparative analysis of all five MoA datasets using a Venn diagram revealed that three MoAs (Abl kinase inhibitor, IKK inhibitor, and PKC activator) were common among all sets; notably, the PKC activator represented the highest MoA count (Fig. 1H). Therefore, the PKC activator was selected for subsequent investigations.

The DEGs of the five sets were further compared with genes whose expression is induced by the PKC activator from the LINCS database to explore the biological relationship between PKC activation and the above-mentioned DEGs (Supplementary Fig. 2a). Among the top 500 PKC activator-induced genes, 126 were upregulated in the five sets. Of these, set2 demonstrated the highest overlap (86 DEGs), followed by set5 (55 DEGs), set3 (43 DEGs), set4 (32 DEGs), and set1 (15 DEGs) (Supplementary Fig. 2b). The number of overlapping DEGs had a similar pattern to that of the counts in the MoA analysis using REMEDY (set2 and set5 had the highest number of DEGs and counts, whereas set1 had the least number of DEGs and counts). The DEGs of the five sets showed a significant degree of connectedness at the individual gene as well as gene class levels (Supplementary Fig. 2c). Comparative Gene Ontology (GO) and pathway enrichment analyses of the five sets revealed multiple terms consistent with PKC activation, including "NGF-stimulated transcription," "regulation of MAPK cascade," "TNF signalling pathway," "FRA pathway," "VEGFA–VEGFR2 signalling," "signalling by receptor tyrosine kinases" and "regulation of wound healing" (Supplementary Fig. 2d). In addition, the enriched cellular components included "cell-substrate junction," "focal adhesion," "protein complex involved in cell adhesion" and "endocytic vesicle" (Supplementary Fig. 2e), reflecting extensive signal transduction activity nearby the cell membrane that could be driven by activated kinases such as PKC. Two DEGs (HB-EGF and EGR2) with the PKC activator-induced signatures were consistently shared across all five sets. Interestingly, this result is consistent with our previous finding that HB-EGF is the primary factor inducing glucose excretion in the intestine. On the other hand, among the downregulated DEGs across the five sets, 11 overlapped with the top 500 PKC activator-induced genes (Supplementary Fig. 3). This pattern is consistent with the overall DEG distribution, wherein upregulated genes substantially outnumbered downregulated ones, suggesting that the treatment predominantly activates—rather than suppresses—biological pathways, including those associated with PKC signalling. Overall, our transcriptome-based molecular signature analysis, empowered by GO and pathway analyses, robustly identifies PKC activation as a top-ranked MoA across the five sets.

Among the PKC activators, ingenol significantly upregulated GLUT1 expression in vitro; however, its high toxicity in vivo precluded further development[19,20]. In contrast, prostratin (12-deoxyphorbol-13-acetate) demonstrated superior pharmacological properties,

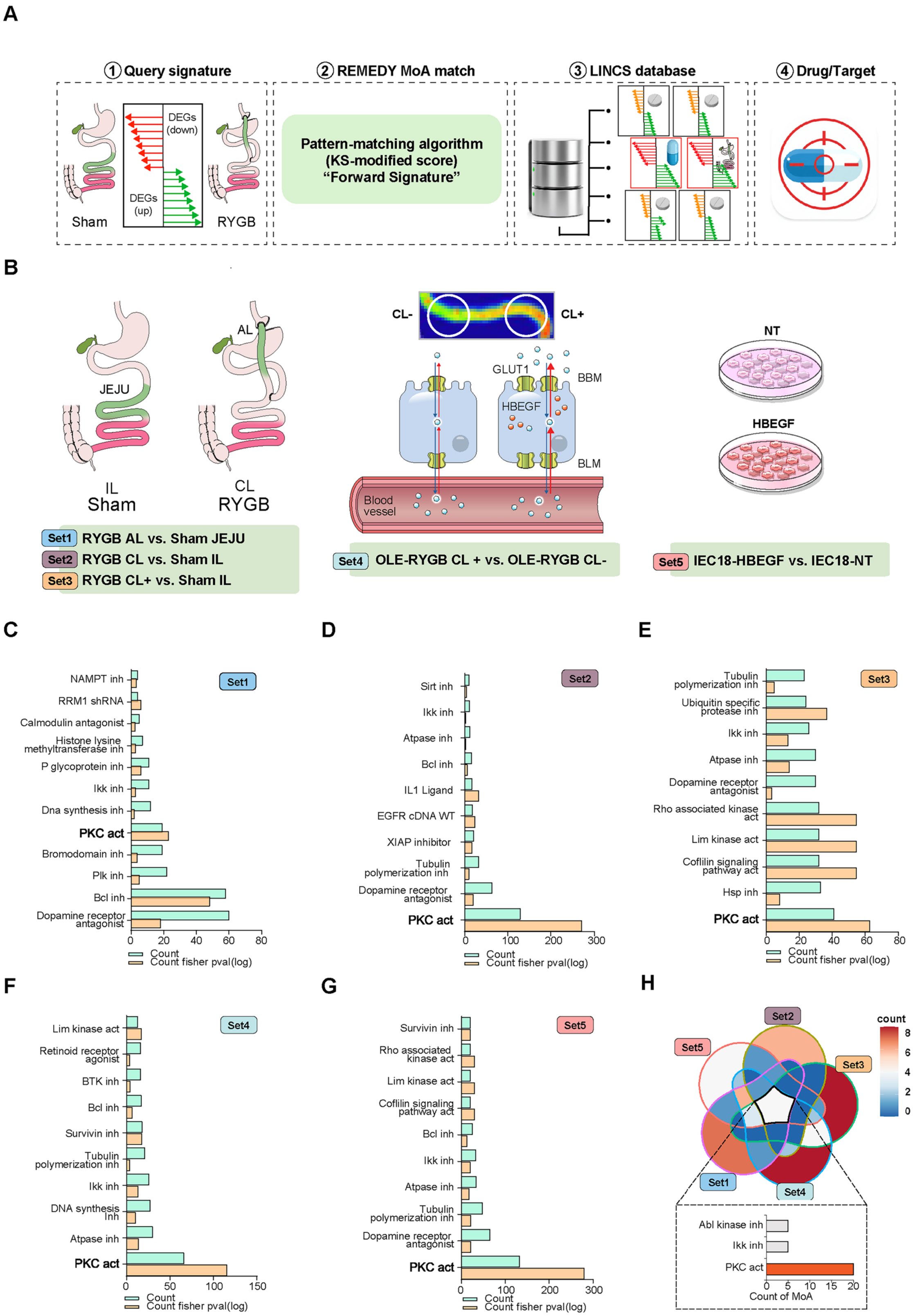

Fig. 1 | Connectivity map-based drug/target identification. A Schematic workflow of the computational drug screening process. Firstly, DEGs were used as query signatures. By detecting the highest similarity using the pattern-matching algorithm (KS-modified algorithm), the best candidates of mechanisms of action (MoAs) showing higher positive connectivity scores can be screened out among signatures in the LINCS database (drugs in the LINCS database were labelled as MoA). The higher the connectivity scores, the better the similarity matching signatures. By counting the MoAs and statistically ranking them based on two-sided paired Fisher's exact test results, the final candidate can be screened out. **B** Schematic representation of the differentially expressed gene (DEG) collection derived from five pairwise comparisons for drug screening. Set1: RYGB AL (Alimentary limb) vs. sham JEJU (Jejunum), Set2: RYGB CL (Common limb) vs. sham IL (Ileum), Set3: RYGB CL+ (FDG uptake high) vs. sham IL, Set4: RYGB CL+ (FDG uptake high) vs. RYGB CL− (FDG uptake low), Set5: IEC18-*HBEGF* vs. IEC18-NT. **C**–**G** MoA analysis and the identified top 10 MoAs denoted by the count number and −log *P*-value for the five sets. **H** MoAs identified at the intersection of the five comparisons. Abbreviations: inh, inhibitor; act, activator. Source data are provided as a Source Data file.

including favourable efficacy and reduced toxicity. Unlike typical phorbol esters, such as phorbol 12-myristate 13-acetate, which activate PKC but promote tumour formation, prostratin, a natural terpenoid compound, is non-tumour-promoting and activator of PKC[21,22].

The PKC family comprises three subfamilies: atypical (aPKCs; PKCζ and PKCλ), conventional (cPKCs; PKCα, PKCβ and PKCγ), and novel (nPKCs; PKCδ, PKCε, PKCη and PKCθ)[23,24]. The aPKCs differ from the other subfamilies in that they lack functional C2 and C1 domains, which account for their insensitivity to Ca^{2+} and diacylglycerol[25,26]. Additionally, aPKCs increase glucose uptake in several peripheral tissues[27–29]. The strong correlation between aPKC and RYGB-induced changes in DEG expression patterns led us to hypothesise that aPKC plays a critical role downstream of the EGFR signalling axis in triggering intestinal glucose excretion.

aPKC upregulates GLUT1 activity in intestinal cells

To investigate the specific cell populations and associated molecular characteristics in the small intestine following RYGB, we performed single-cell transcriptome profiling (scRNA-seq) on Otsuka Long-Evans Tokushima Fatty (OLETF) sham jejunal and ileal tissues, as well as on RYGB AL and CL tissues. We identified eight main cell types, namely enterocytes, goblet cells, enteroendocrine cells, endothelial cells, immune cells, and fibroblasts, each defined by canonical marker genes (Fig. 2A). Notably, RYGB-operated limbs exhibited significantly increased enterocyte populations (Fig. 2A). We also analysed the expression patterns of *Hbegf*, *Slc2a1* (*GLUT1*), *Hk2*, and *aPKC* in both sham- and RYGB-operated rat small intestines using scRNA-seq and observed that *Hbegf* and *Prkcz* were upregulated in the proximal and distal enterocyte cell clusters (Fig. 2B). Consistent with our total RNA-seq results in RYGB samples, we observed that aPKC was overexpressed in the RYGB distal enterocyte cell cluster when compared with that in sham distal enterocyte cells (Fig. 2C and Supplementary Fig. 4a, b). Furthermore, RYGB CL exhibited elevated aPKC protein levels compared to the sham IL according to immunoblot analysis (Supplementary Fig. 4c), whereas aPKC protein levels in the colon were comparable between the RYGB and sham groups (Supplementary Fig. 4d). Additionally, HB-EGF treatment of the intestinal epithelial cells (IEC) induced aPKC translocation to the plasma membrane, concomitant with GLUT1 translocation (Supplementary Fig. 4e).

To understand the molecular characteristics associated with these differences, we performed gene set enrichment analysis. Consistent with previous findings[30,31], the aPKC high-expressing cell clusters exhibited increased expression of gene sets related to tight junction interactions and cell–cell communication (Supplementary Fig. 4f). In particular, the aPKC high-expressing cell clusters were associated with gene expression patterns related to improved glucose tolerance and decreased body fat phenotypes in mice (Supplementary Fig. 4g). Moreover, these cell clusters shared a differential gene expression pattern with EGFR (Supplementary Fig. 4h). Collectively, our bulk and single-cell transcriptomic profiles led us to hypothesise that aPKC is crucial for the distal intestinal glucose excretion effect downstream of the EGFR pathway.

To determine whether prostratin can phosphorylate endogenous and/or overexpressed aPKC isozymes in cells, we used an aPKC-specific C kinase activity reporter (aCKAR) flanked by a fluorescence resonance energy transfer (FRET) pair (cyan fluorescent protein [CFP] and yellow fluorescent protein)[32]. IEC transfected with aCKAR and the PKCζ plasmid exhibited increased aCKAR activity compared with empty plasmid-transfected cells. Both the empty-plasmid and PKCζ-overexpressing cells exhibited increased aCKAR activity after prostratin treatment (Fig. 2D). Furthermore, our in vitro kinase assay results revealed a prostratin dose-dependent increase in aPKC activity (Fig. 2E).

aPKC reportedly plays a crucial role in translocating glucose transporters to the plasma membrane in muscle and adipose tissues[32–35]. To investigate whether aPKC can increase intestinal GLUT1 localisation to the plasma membrane, we overexpressed PKCζ in IEC and observed significantly increased cell surface expression of GLUT1 as compared with that in control cells (Fig. 2F). 2-deoxy-D-glucose (2-DG) uptake was also significantly higher in the PKCζ-overexpression IEC than in control IEC (Fig. 2G). In agreement with the results from the PKCζ overexpression experiments, prostratin treatment induced increased GLUT1 activity in both IEC and human intestinal organoids (Fig. 2H, I and Supplementary Fig. 5a, b).

To investigate the role of aPKC in prostratin-induced GLUT1 translocation, we used CRISPR to generate IEC that lacked the cPKC (PKCα), nPKC (PKCδ) or aPKC (PKCζ and PKCι) isoforms (Supplementary Fig. 5c). Each isoform was selected based on its highest expression level among subtypes in the human intestine and OLETF RNA-seq results (Supplementary Fig. 5d). Prostratin treatment significantly increased GLUT1 phosphorylation in all groups except for the aPKC knockout (KO) group, suggesting that aPKC plays a crucial role in prostratin-induced GLUT1 translocation (Fig. 2J and Supplementary Fig. 5e). Furthermore, the 2-DG uptake experiments revealed that only aPKC KO cells exhibited attenuated effects of prostratin. Conversely, PKCα cells exhibited upregulated basal 2-DG uptake, and PKCδ cells demonstrated unaltered prostratin sensitivity (Fig. 2K).

Subsequently, we treated IEC with prostratin alone or in combination with ζ-inhibitory peptide (ZIP). The addition of ZIP inhibited prostratin-induced glucose uptake in IEC (Fig. 2L). Therefore, our findings confirm that aPKC activation upregulates GLUT1 phosphorylation and promotes subsequent glucose uptake by intestinal cells, which mimics the increased glucose uptake observed in the distal intestine post-RYGB surgery.

aPKC enhances glucose efflux via cell surface GLUT1 translocation

To assess whether aPKC induces GLUT1 translocation to the cell surface and consequently regulates glucose uptake in IEC and intestinal organoids, we performed flow cytometry to monitor the functional expression of GLUT1 and evaluate its functional capacity. aPKC overexpression increased GLUT1 cell surface translocation in both IEC6 and IEC18 (Fig. 3A, B). In IEC, prostratin treatment significantly increased GLUT1 cell surface translocation compared with that in the control group (Fig. 3C). However, this effect was abolished in aPKC KO cells (Fig. 3C).

We stained human intestinal organoids with phalloidin, an apical marker, to visualise the apical membrane. In prostratin-treated organoids, GLUT1 colocalised with villin and migrated to both the basolateral and apical membranes (Fig. 3D and Supplementary Fig. 6). Intestinal organoids treated with prostratin and the PKCζ inhibitor peptide ZIP exhibited decreased GLUT1 translocation when compared with those treated with prostratin alone (Fig. 3D and Supplementary Fig. 6). These findings suggest that aPKC overexpression and/or prostratin treatment can lead to GLUT1 translocation to the intestinal cell membrane.

To evaluate the effect of prostratin on intestinal glucose excretion, we performed glucose and fluorescein isothiocyanate (FITC)-dextran tracer assays. The IEC18 cell lines that stably overexpressed aPKC exhibited elevated glucose excretion compared with that in control cells (Fig. 3E). Similarly, prostratin treatment induced glucose excretion; conversely, treatment with STF-31, a GLUT1-specific inhibitor, abolished this effect in IEC (Fig. 3F). Glucose excretion was also increased by prostratin treatment in intestinal organoids (Fig. 3G). These results indicate that aPKC-mediated GLUT1 cell surface translocation plays a crucial role in increased glucose efflux.

To investigate the effects of PKCζ and prostratin on glucose metabolism in IEC, we evaluated glycolytic activity by measuring the extracellular acidification rate (ECAR). Experiments were performed

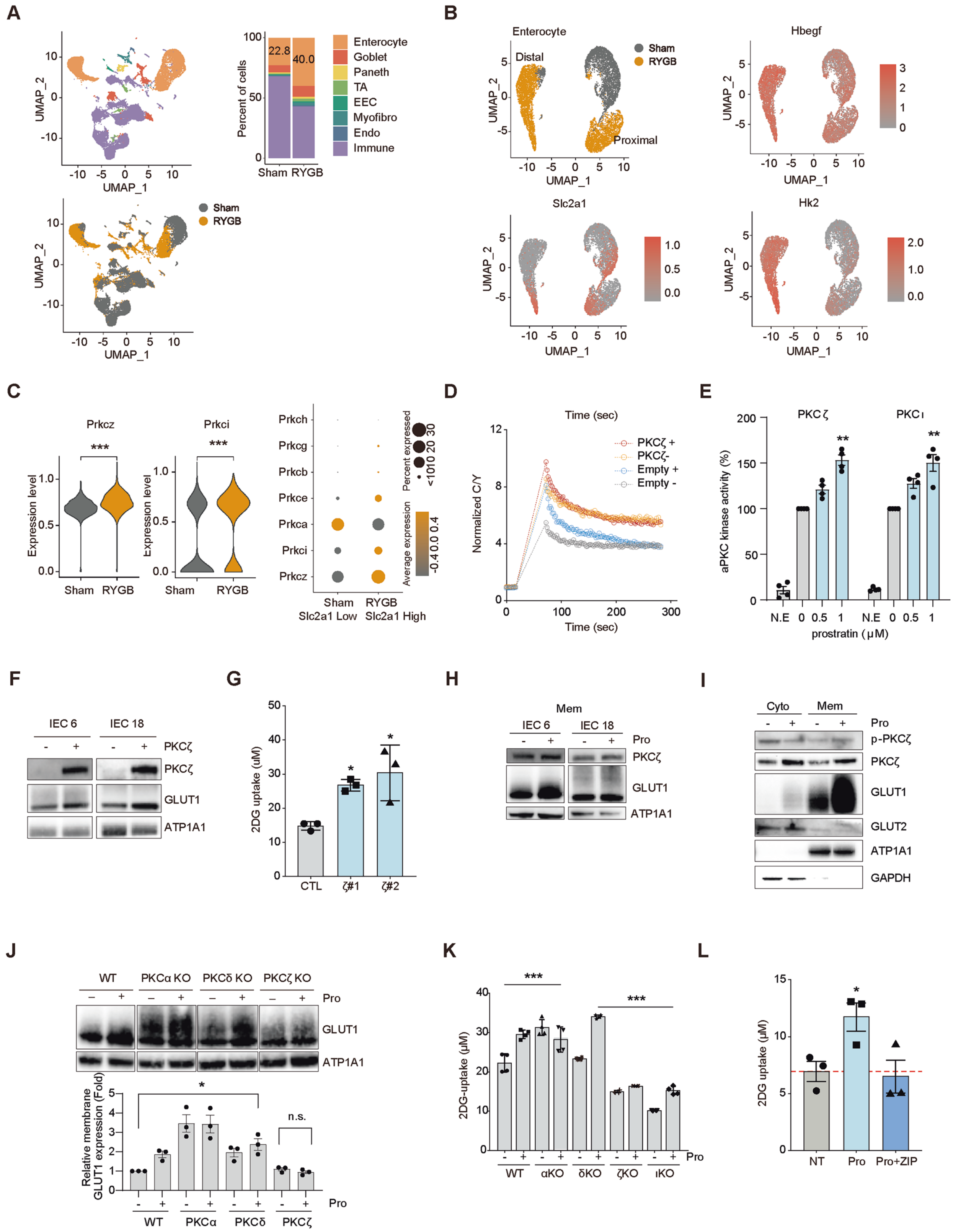

with and without PKCζ overexpression (Fig. 3H) and in the presence of prostratin at concentrations of 0.5, 1, and 5 μM (Fig. 3I). Notably, despite increased GLUT1 expression in PKCζ-overexpressing IEC, no significant differences in ECAR were observed, suggesting minimal impact on glycolysis. Similarly, at prostratin concentrations that induced glucose excretion, ECAR remained comparable to that of the untreated group. These findings support the hypothesis that aPKC-mediated GLUT1 upregulation promotes glucose efflux rather than enhancing glycolysis.

Intestinal aPKC activation mimics RYGB-mediated glycaemic control in diabetic mice

After observing the intestinal glucose excretion effect of aPKC activation in vitro, we investigated this phenomenon further in a high-fat

Fig. 2 | Characterisation of small intestinal cell landscape and PKCζ-mediated regulation of glucose uptake in vitro and ex vivo. **A** UMAP plots depicting the landscape of small intestine cells of sham- and RYGB-operated OLETF rats (Left). Cells are coloured according to the clustering result. Enterocyte cell type populations are numbered (Right). EEC enteroendocrine cells, Endo endothelial cells, Immune immune cells, Myofibro fibroblasts. **B** UMAP plots depicting enriched *Hbegf*, *Slc2a1* (GLUT1), and *Hk2* expression in the enterocyte cluster. **C** (Left) Violin plots of *Prkci* (PKCλ) and *Prkcz* (PKCζ) expression in the distal intestine enterocyte cluster. (Right) Dot plot indicating the expression and percentage of PKC subfamily genes of distal enterocytes in sham (*Slc2a1* Low) and RYGB (*Slc2a1* High). *** $P < 0.001$, two-tailed Student's *t*-test. **D** IEC was co-transfected with empty or PKCζ plasmids and aCKAR. The CFP/yellow fluorescent protein FRET (C/Y) emission ratio was quantified as a function of time after the addition of prostratin (5 µM). Data are presented as mean ± SEM from $n \geq 15$ cells. **E** Kinase activity of purified PKCζ measured in the presence of 0–1 µM prostratin ($n = 4$, independent experiments). **F** Immunoblots of plasma membrane lysates of IEC6 and IEC18 cells transfected with empty or PKCζ-expressing plasmids after 48 h. GLUT1 expression is normalised to that of Na^+/K^+ ATPase (ATP1A1). **G** 2-DG uptake in control and PKCζ-overexpressing clones (clone #1 and clone #2). ($n = 3$, independent experiments) **H** Immunoblots of IEC6 and IEC18 lysates after prostratin (+) or DMSO (−) treatment. Expression was normalised to that of Na^+/K^+ ATPase (ATP1A1). **I** Immunoblots of cytoplasm (Cyto) and plasma membrane (Mem) lysates of human intestinal organoids treated with prostratin or DMSO. Expression was normalised to that of GAPDH for Cyto and ATP1A1 for Mem. **J** Immunoblots of plasma membrane lysate and bar graph of IEC18 WT, PKCα KO, PKCδ KO, PKCζ KO, and PKCι KO cells. Expression was normalised to that of ATP1A1 ($n = 3$, independent experimenst, two-tailed Student's *t*-test). **K** 2-DG uptake in IEC18 WT, PKCαKO, PKCδKO, PKCζKO and PKCιKO cells treated with Pro (+) or DMSO (−). ($n = 4$, independent experiments, Kruskal–Wallis test with Dunn's post-hoc test). **L** 2-DG uptake in IEC18 cells treated with DMSO, Pro, or Pro + ZIP. ($n = 3$, independent experiments). All data are presented as mean ± SEM. Data in (**F**, **H**, **I** and **J**) show representative immunoblots from three independent experiments; all yielded reproducible results. Data in (**E**, **G**, **I** and **L**) were analysed using two-sided Mann–Whitney *U* test; *$P < 0.05$, **$P < 0.01$, ***$P < 0.001$, n.s. non-significant vs. NT, CTL, or WT (−). Source data are provided as a Source Data file.

diet-induced obesity (DIO) mouse model. We constructed expression vectors for the PKCζ protein and administered PKCζ or control vectors complexed in a polyethylenimine-based gene delivery solution to DIO mice via repeated injections (Fig. 4A and Supplementary Fig. 7a). In an independent pilot study, we observed stable PKCζ protein expression in the small intestine and colon in vivo. Specifically, PKCζ-overexpressing mice gained weight later than control mice did (Fig. 4B). Fasting blood glucose levels were also significantly decreased in PKCζ mice (Fig. 4C). Intraperitoneal glucose tolerance tests revealed significantly enhanced glucose tolerance in response to PKCζ overexpression (Fig. 4D).

To determine whether PKCζ enhances intestinal glucose uptake and excretion, FDG was injected into the tail vein of mice, and the amount of excreted FDG in their gastrointestinal tracts was measured. Our findings indicated that FDG uptake was higher in the distal small intestine and colon of PKCζ mice than control mice (Fig. 4E and Supplementary Fig. 7b). Post-lavage fluids from the small intestine and colon were isolated and analysed for radioactivity; we observed higher FDG excretion in the PKCζ group compared with that in the control group (Fig. 4F). Serum insulin levels as well as homeostatic model assessment of insulin resistance and homeostatic model assessment of β-cell function were not significantly different between the PKCζ and control mice (Supplementary Fig. 7c). These results suggest that the delayed body weight gain and improved glucose homeostasis observed in PKCζ mice were independent of changes in insulin levels.

The relationship between the PKCζ, metabolic profile, and GLUT1 expression in the ileum and colon was analysed. We observed a significant positive correlation between PKCζ expression in DIO mice and GLUT1 protein expression in both tissues (Fig. 4G). Furthermore, a significant positive correlation was observed between PKCζ expression and FDG uptake. In contrast, PKCζ expression in the ileum and colon was negatively correlated with blood glucose levels and body weight gain in DIO mice (Fig. 4G). Additionally, GLUT1 expression was significantly higher in the ileum and colon of PKCζ mice than in the ileum and colon of control mice (Fig. 4H). Immunohistochemical staining for PKCζ and GLUT1 also revealed stronger staining for GLUT1 in the ileum and colon of PKCζ mice, confirming its effect on intestinal glucose excretion (Fig. 4I, J and Supplementary Fig. 7d). Notably, GLUT1-positive cells in the ileum and colon exhibited different staining patterns, with immunoreactivity localised to the cytoplasmic and basolateral membranes of enterocytes in the ileum of PKCζ mice, whereas it localised to the apical and basolateral membranes of enterocytes in the colon.

To investigate whether intestinal aPKC, rather than aPKC in other metabolic organs, drives reduced body weight and improved glucose homeostasis, we injected Cre-dependent adeno-associated virus (AAVs) expressing aPKC (AAV9-Flexon-aPKC) or GFP (AAV-Flexon-GFP) into the tail vein of male Villin-Cre mice (Supplementary Fig. 8a). Efficient aPKC overexpression was confirmed based on the elevated intestinal protein levels of PKCζ and PKCλ, with no increases observed in other metabolic organs, such as the liver or brown adipose tissue (Supplementary Fig. 8d). Under a high-fat diet, aPKC-overexpressing mice exhibited delayed body weight gain and enhanced glucose homeostasis compared to GFP controls (Supplementary Fig. 8b, c).

Metabolic cage experiments showed a slight, non-significant increase in the respiratory exchange ratio (RER) in aPKC-overexpressing mice (Fig. 4K and Supplementary Fig. 8e, f), with no significant differences in physical activity, heat production, or food intake (Fig. 4L–N). Plasma insulin and GLP-1 levels did not differ significantly between groups (Supplementary Fig. 8g, h). These findings indicate that intestinal aPKC plays a critical role in reducing body weight and improving glucose homeostasis, likely through enhanced intestinal glucose efflux.

Prostratin treatment mimics RYGB-mediated glycaemic control in diabetic mice

Lastly, we investigated the effects of prostratin on db/db mice. Treatment with prostratin significantly reduced weight gain (Fig. 5A) and markedly enhanced glucose tolerance response (Fig. 5B, C) as compared to treatment with the vehicle. Prostratin-treated mice had higher FDG uptake in the duodenum, jejunum, and ileum (Fig. 5D, E) and exhibited enhanced glucose excretion following lavage (Fig. 5F).

Given the unique mechanism of glycaemic prostratin function, we assessed its efficacy in mice with deficient insulin signalling induced by streptozotocin injection (mice with STZ-induced diabetes). These mice received daily injections of either prostratin or vehicle for one week. Autoradiography and gamma count results demonstrated markedly increased intestinal FDG uptake in prostratin-treated mice when compared with that in vehicle-treated mice (Supplementary Fig. 9a, b). Furthermore, prostratin-treated mice showed enhanced FDG excretion (Supplementary Fig. 9c).

Transmission electron microscopy confirmed that prostratin treatment did not affect intestinal microvilli length or enterocyte tight junction integrity (Fig. 5G and Supplementary Fig. 9d). Immunohistochemistry confirmed that prostratin-treated mice exhibited increased jejunal and ileal PKCζ apical membranous villus expression when compared with vehicle-treated mice (Fig. 5H, I). In addition, prostratin-treated mice demonstrated upregulated GLUT1 expression extending from the proximal to distal small intestine (Fig. 5H, I and Supplementary Fig. 9e).

To investigate prostratin's effect on food intake and exclude reduced appetite as a potential confounder for the observed

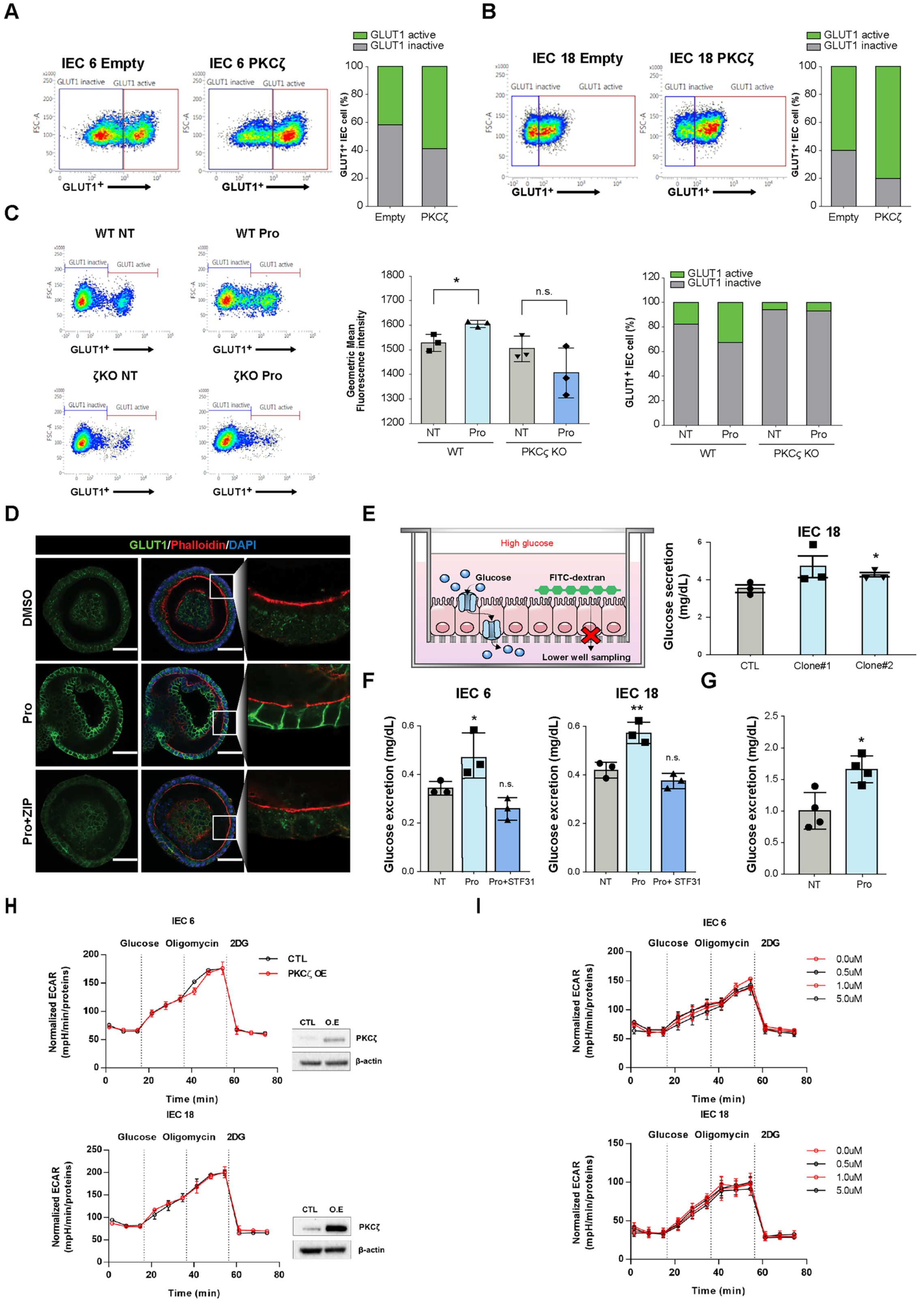

improvements in body weight and glucose homeostasis, we monitored RER, food intake, body heat production, and physical activity over a 72-h period. No significant differences were observed in food intake, body heat production, or locomotor activity between the prostratin and vehicle groups (Fig. 5J–L). Collectively, these results suggest that prostratin effectively reduces weight gain and improves glucose homeostasis by activating the PKCζ/GLUT1 signalling pathway, thereby triggering glucose uptake and excretion in the intestinal tract.

Discussion

Genome-wide association studies can identify risk-associated loci for diseases. However, a partial list is generally insufficient for establishing causality and providing mechanistic insights. Understanding cellular

Fig. 3 | aPKC-induced surface GLUT1 expression increases glucose efflux. Representative flow cytometric dot plot depicting the cell population with cell surface expression of GLUT1 in empty or PKCζ plasmid-transfected **A** IEC6 and **B** IEC18 cells. The blue and red squares represent the gating strategy used to sort GLUT1-inactive and GLUT1-active cells within the IEC. Right bar graph displays the cumulative frequency of cells based on their cell surface expression of GLUT1. **C** Representative flow cytometric dot plot displaying the cell population with cell surface expression of GLUT1 in WT or PKCζ cells treated with either PBS (NT) or prostratin (Pro). Left bar graph depicting geometric mean fluorescence intensity. Right bar graph depicting the cumulative frequency of cells based on their cell surface expression of GLUT1. (Data **A**–**C**, $n = 3$, independent experiments) **D** Immunofluorescence staining of GLUT1 and phalloidin in human organoids treated with DMSO (NT), prostratin 3 µM (Pro), or Pro + ZIP 1 µM. Immunofluorescence staining of GLUT1 (Alexa 488, green), phalloidin (Alexa594, red), and membrane colocalisation (Scale bar = 50 µm, $n = 3$ samples, independent experiments). **E** Upper: Schematic illustration of the glucose excretion assay procedure. High glucose (25 mM with FITC-dextran) was added to the upper well. Samples were collected in the lower well. The levels of both glucose and leaked FITC-dextran were measured. Lower: Comparison of glucose excretion in the lower well of WT and PKCζ-overexpressing clones #1 and #2 after adding high glucose (25 mM) to the upper well (Data **E** and **F**, $n = 3$, independent experiments). Comparison of glucose execretion in the lower well of (**F**) IEC treated with NT, Pro, or Pro + ZIP, and (**G**) mouse organoids treated with NT or Pro. (n = 4, independent experiments). **H** ECAR assays indicated no difference between control (CTL) and PKCζ-overexpressing (PKCζ OE) IEC. **I** ECAR assays indicated no significant difference in prostratin-treated IEC (Data in **H** and **I**, $n = 3$, independent experiments, one-way ANOVA followed by Dunnett's multiple comparisons test). All data are presented as the mean ± SEM. Data in (**C**, **E**, **F** and **G**) were analysed using Student's *t*-test; $^{*}P < 0.05$, $^{**}P < 0.01$, n.s. non-significant vs. NT or CTL. Source data are provided as a Source Data file.

functions requires perturbing the system, i.e., modulating the target and monitoring consequences. CMap, which connects genes, drugs, and diseases using common gene expression signatures, can be used to elucidate the mechanisms of action of small molecules. In this study, we used REMEDY (developed based on CMap) to screen potential candidate drugs to elucidate the pathological mechanisms and identify therapeutic options for hyperglycaemia. We screened against the LINCS L1000 database, thereby identifying PKC activators as potential drivers of intestinal glucose excretion and glycaemic control in the non-glucose-excreting intestine. We further confirmed that aPKC is crucial for the intestinal glucose excretion effect observed after gastric bypass surgery, facilitating serum glucose uptake and excretion by the distal intestine to improve glucose homeostasis. Prostratin, an aPKC activator and non-tumour-promoting natural compound, induced intestinal glucose excretion in the distal intestine and enhanced glucose homeostasis.

In recent years, L1000 Fireworks Display (L1000FWD), the Drug Gene Interaction Database, and CMap have been used to predict the effect of existing small drugs by comparing the DEGs in various diseases[16]. This strategy has been applied successfully to cancer[36], muscle atrophy[37], acute myelogenous leukemia[38], and Parkinson's disease[39]. We report the application of the LINCS L1000 CMap database to diabetes, demonstrating its ability to identify potential drugs/targets for intestinal glucose excreting and non-excreting tissues.

Analysis of individual PKC isoforms revealed that intestinal glucose excretion was sensitive to PKCζ and PKCι. Deletion of other PKC isoforms, in contrast, induced increased intestinal glucose excretion, suggesting that intestinal glucose excretion depends on specific PKC isoforms. Similar to the findings of previous studies on the role of aPKC in peripheral tissues, the intestinal tissue-specific effect of aPKC induces glucose uptake, leading to decreased blood glucose levels. aPKC can be activated through exercise-induced AMPK activation, which leads to increased glucose uptake in muscle cells via the activation of GLUT4 transporters[40,41]. aPKC activation regulates GLUT4 transporter activation and promotes glucose uptake in adipocytes[42]. In the small intestine, aPKC regulates the activity of insulin-independent GLUT1, unlike in skeletal muscle or adipocytes, where insulin-dependent GLUT4 is primarily responsible for glucose uptake[27]. Therefore, the functional expression of aPKC-activated glucose transporters may vary between tissues.

Extensive evidence from previous studies support our findings, demonstrating the importance of the intestine in the glucose-lowering effect of GLUT1[8,11]. Metformin, the most widely prescribed drug for type 2 diabetes mellitus, upregulates intestinal GLUT1 to exert its glucose-lowering effect[43,44]. Specifically, metformin also induces glucose deposition in the intestinal lumen; however, the underlying mechanism remains unclear[45–48].

Unlike the structurally related phorbol esters, prostratin is not a tumour promoter or an irritant; instead, it protects against the tumour-promoting effects of these agents[21,49,50]. As metformin acts as an anticancer drug[51,52], we speculated the existence of a minor association between intestinal GLUT1 and neoplasms. Similarly, no hyperplasia was observed in cell cultures, mice, or human organoids treated with prostratin. Moreover, the results of our GO analysis of DEGs in PKCζ-overexpressing IEC and the ileum of DIO mice revealed significant upregulation of the p53 tumour suppressor pathway (Supplementary Fig. 10c, d). This finding suggests a complex interplay between aPKC and GLUT1 activation, potentially through a non-canonical pathway, in addition to the hypothesised EGFR signalling mechanism.

In our single-cell analysis of the distal intestine of RYGB-operated mice, gene set enrichment analysis of the aPKC-expressing enterocyte cluster revealed DEGs related to improved glucose tolerance and decreased body weight; EGFR was identified as a high-rank hub protein, and IEC treated with EGFR ligand activated PKC (Supplementary Fig. 4e–h). Collectively, these findings suggest that intestinal aPKC activity plays a crucial role in glucose homeostasis and body weight control downstream of the EGFR hub. Notably, we also observed improved gut barrier integrity in aPKC high-expressing enterocyte clusters, as evidenced by upregulated gene sets related to tight junction interactions and cell–cell communications (Supplementary Fig. 4f). These morphological and functional changes suggest that aPKC activation not only facilitates glucose excretion but also promotes epithelial proliferation and reinforces intestinal barrier function without inducing oncogenic hyperplasia.

Prostratin is currently being tested in a clinical trial for HIV eradication based on its activity on PKC[21,49,50]. Prostratin also plays a role in the membrane translocation of aPKC[50,53]. Prostratin-induced aPKC activation in the small intestine can increase serum glucose uptake (Figs. 5D and 5E). APKC KO intestinal cells showed reduced prostratin-induced GLUT1 expression and glucose uptake (Fig. 2J and K). The unique action of prostratin on glucose uptake and secretion is attributed to its selective induction of GLUT1, with no significant impact on other glucose transporters, such as GLUT2 (Fig. 2I). GLUT1 is crucial for prostratin-mediated glucose uptake and secretion (Figs. 2G, L and 3F, G). In STZ-induced diabetic mice (model of type 1 diabetes), prostratin enhanced FDG uptake into the intestinal tissue and increased FDG excretion from the intestine (Supplementary Fig. 9a–c). Our findings demonstrate that prostratin reduces body weight and improves glucose homeostasis without altering food intake, ruling out reduced appetite as a confounding factor (Fig. 5J–L). Instead, prostratin activates the PKCζ/GLUT1 signalling pathway, enhancing glucose uptake and excretion in the intestinal tract. These results highlight a gut-specific mechanism underlying prostratin's metabolic benefits.

The differential spatial patterns of FDG uptake observed between PKCζ overexpression and prostratin treatment highlight distinct physiological mechanisms (Fig. 4D vs. Fig. 5D). PKCζ overexpression predominantly enhanced FDG uptake in the distal small intestine (ileum) and colon, consistent with higher baseline PKCζ

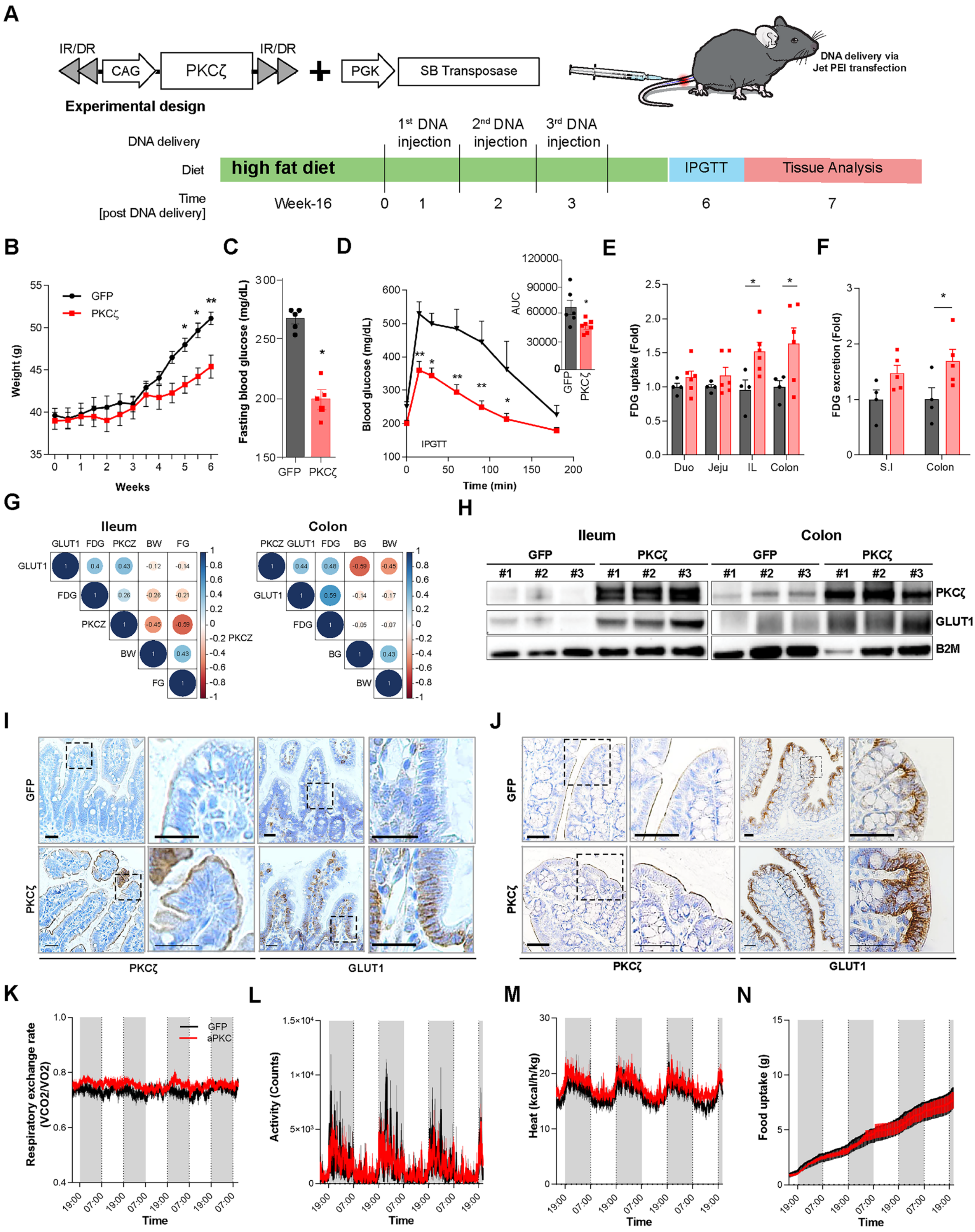

expression in these regions, as evidenced by elevated *Prkcz* levels in distal enterocytes post-RYGB (Fig. 2C). In contrast, prostratin treatment increased FDG uptake uniformly across the duodenum, jejunum, and ileum (Fig. 5D), likely due to its pharmacological activation of both PKCζ and PKCι, and potentially other PKC isoforms, resulting in broad GLUT1 upregulation (Fig. 5H, I and Supplementary Fig. 9e).

Prostratin induces GLUT1 expression on both the apical and basolateral sides, suggesting that GLUT1 plays a role in absorbing plasma glucose into enterocytes and activating glucose utilisation, as well as excreting high concentrations of glucose from enterocytes into the luminal space through apical GLUT1 expression, thereby facilitating glucose disposal. This was confirmed by autoradiography and gamma count experiments in aPKC-overexpressing mice and

Fig. 4 | Intestinal aPKC activation enhances intestinal glucose excretion in diabetic mice. A Schematic illustration of the experimental procedure and timeline. Selected transposons were delivered with JetPEI with plasmids encoding transposase. **B** Effect of PKCζ overexpression on body weight compared with that of the control (GFP) treatment in diet-induced obesity (DIO) mice. **C** Fasting blood glucose level of GFP and PKCζ. **D** Intraperitoneal (i.p.) glucose tolerance tests (Data in (**B**–**D**), $n = 5–6$ mice per group). **E** 2-deoxy-2-[^{18}F]-fluoro-D-glucose (FDG) biodistribution analysis in PKCζ and GFP mice revealing higher FDG uptake in the intestine of PKCζ mice. (Data in **E**, and **F**, $n = 4–6$ mice per group). **F** Small intestinal (S.I) and colonic lumen phosphate-buffered saline (PBS) washing analysis. Intestinal lumen PBS washings revealed increased FDG excretion in PKCζ mice. (Data in **E** and **F**, $n = 4–5$ mice per group). **G** Correlation analysis between PKCζ expression and GLUT1; Spearman's correlation analysis for blood glucose (BG), body weight (BW) and FDG uptake in ileal and colonic tissues. **H** Immunoblots of ileal and colonic tissue lysates from GFP- or PKCζ-expressing mice. The expression level was normalised to that of beta-2-microglobulin (B2M), $n = 3$ per group. Representative images of PKCζ and GLUT1 immunostaining in the **I** ileal and **J** colonic tissues of GFP or PKCζ mice ($n = 3$ per group). Scale bar = 25 µm (**H**) and scale bar = 50 µm (**I**). **K**–**N** Villin-Cre mice expressing aPKC or GFP were placed into metabolic cages for 72 h to measure average ($n = 4$ mice per group). **K** Respiratory exchange ratios (RER, VCO$_2$/VO2), **L** Activity level (Counts), **M** Body heat (kcal/h/kg), and **N** Food consumption. All data are presented as the mean ± SEM. Data in (**B**, **D**, **E**, and **F**) were analysed using two-way ANOVA followed by Sidak's multiple comparisons test and (**C**) were analysed using two-sided Mann–Whitney *U* test; $^{*}P < 0.05$, $^{**}P < 0.01$ vs. GFP. Source data are provided as a Source Data file.

prostratin-treated db/db mice. GLUT1 overexpression in the apical and basolateral membranes possibly provides enterocytes with the required glucose for intestinal hypertrophy. However, being a bilateral transporter, GLUT1 overexpression results in more serum glucose diffusion into the intestinal lumen as the overall glucose gradient nearly always favours serum-to-lumen excretion. The overall dynamics of this glucose flux are reflected in the autoradiograph analysis results, which revealed increased glucose availability in the enterocytes based on post-washing autoradiography, and the collected glucose (in the form of FDG) in the intestinal lavage revealed increased serum glucose excreted into the intestinal lumen.

Recently, GLP-1 receptor agonists have emerged as an effective treatment option for individuals with type 2 diabetes[54]. These agents function by enhancing insulin secretion, reducing glucagon secretion, slowing gastric emptying, and promoting satiety primarily through receptor binding in the hypothalamus and hindbrain. Combining prostratin with GLP-1 receptor agonists may offer complementary mechanisms of action to address the pathophysiologic defects associated with type 2 diabetes. Such a combination could potentially result in timely glycaemic control and additive cardiovascular and renal benefits.

A major limitation of our study is the lack of an existing aPKC-specific activator. Although cPKC and nPKC inhibitors have been developed to target diabetic retinopathy, neuropathy, and cancer, we currently lack a specific activator for aPKC. Nonetheless, we confirmed that aPKC-mediated glucose uptake and secretion could be induced in vitro and in vivo by inducing aPKC overexpression or via CRISPR KO studies. As there is no selective aPKC activator, we could not evaluate the effect of an aPKC-selective activator in vivo. To address this limitation, several strategies were employed. We utilised the Sleeping Beauty transposon gene delivery system to overexpress PKCζ in the intestine. The rationale for exclusively investigating the effects of PKCζ overexpression in vivo can be attributed to two main reasons: first, based on single-cell sequencing, a significant correlation was observed between the glucose excretion effect in the intestine after bariatric surgery and aPKC expression with PKCζ expression. In our comparative analysis of RNA sequencing data from PKCζ^{+} IEC18 cells, PKCζ^{+} DIO mouse ileal tissues, and RYGB-operated high-FDG uptake CL tissues, common activation of the EGFR signalling pathway was observed (Supplementary Fig. 10a, b). REMEDY analysis consistently identified the presence of PKC activators in these samples (Supplementary Fig. 10e, f). Second, when PKCζ and PKCι were overexpressed individually or in combination in intestinal cells, no synergistic effect was observed, but rather a mild additive effect, suggesting similar roles for these two subtypes (Supplementary Fig. 11a–c).

In conclusion, our findings confirmed that aPKC overexpression in the small intestine enhances serum glucose uptake into enterocytes and its subsequent excretion from enterocytes to the intestinal lumen via GLUT1 upregulation. This mechanism of aPKC activation provides insights into the future development of antidiabetic and weight loss drugs.

Methods

Ethics approval

The research reported here complies with all relevant ethical regulations and guidelines. Small intestine tissue biopsies used in this study were obtained from patients who provided written informed consent under the ethical committee of Severance Hospital (IRB: 4-2019-1173). Animal experiments were performed in accordance with the regulations of the Institutional Animal Care and Use Committee of Severance Hospital, Seoul, Republic of Korea (2021-0287). Human intestinal tissues used for organoid culture were obtained under Institutional Review Board approval and were processed for experimental analysis.

DEG collection from five pairwise comparisons

To search for potential drugs/targets that are able to mimic the serum glucose excretion effect, transcriptome data from five different pairwise comparisons of glucose excretion and non-glucose excretion tissue/cells were collected, and the DEGs were determined. Three comparisons are from OLETF rat RYGB-operated glucose excretion tissue and sham-operated non-glucose excretion tissue. These are pair one: RYGB AL vs. sham, jejunum part (sham JEJU) (DEG was collected by log2FC ≥ 2 & $P < 0.05$), pair two: RYGB CL vs. sham, ileum part (sham IL) (DEG was collected by log2FC ≥ 1 & $P < 0.05$), and pair three: RYGB CL+ (high-FDG uptake part of CL) vs. sham IL (DEG was collected by $\log_2$FC ≥ 1 & $P < 0.05$). Another comparison involves the high-FDG uptake and low-FDG uptake sections of the intestine in OLETF rats that underwent RYGB, indicated as pair four: RYGB CL+ vs. RYGB CL− (DEG was collected by $\log_2$FC ≥ 1 & $P < 0.05$). The last one is from HB-EGF treated and NT cells, indicated as pair five: intestine epithelial cell line (IEC18)-*HBEGF* vs. IEC18-NT (DEG was collected by log2FC > 1).

Drug/target predictions using the LINCS L1000 database

The DEGs generated from five pairwise comparisons above were applied to screen for potential drugs/targets through REMEDY platform. Differential expression signature of Arontier's transcriptomic-mediated drug discovery platform, namely REMEDY, was built based on level four differential expression signature in the LINCS database. These data from LINCS comprise the z-score-normalised form of nearly 1 201 945 differential expression signatures resulting from landmark gene-mediated transcription inference. We downloaded these data from Gene Expression Omnibus database (Phase I: GSE92742, Phase II: GSE70138)[16]. Then, we downloaded the MoA and the clinical phase information of the perturbagens in LINCS from the Drug Repurposing Hub (https://clue.io/repurposing). The expression-based similarity between the query up- and downregulated DEGs and signatures database was achieved using two dependent pattern-matching algorithms, one is the CMap-adopted scoring function, KS[16], and the other one is KS-dependent modified score developed by Arontier company. As all query signatures comprise treatment rather than disease signatures, positive (forward) connectivity scores were only considered for determining potentially repurposing perturbagens. To identify perturbagens with potentially significant repurposing

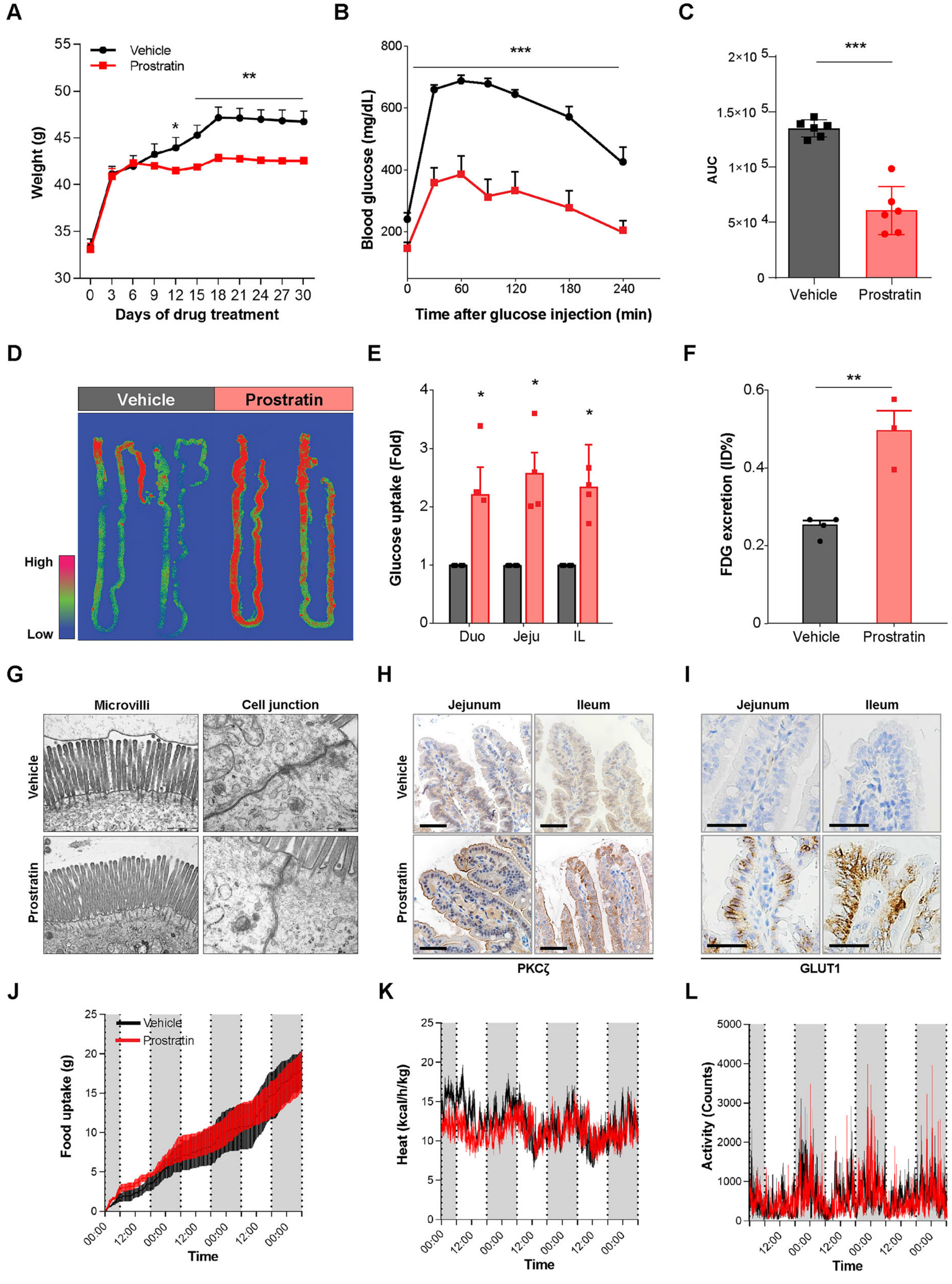

performance, perturbagens were ranked, and the ratio of the count of each perturbagen, regardless of time, concentration, or cell line, among the first 1000 signatures to their count in the total signatures was calculated and statistically assessed using Fisher's exact test of paired data. The same approach was followed when ranking potentially targeted MoAs. A number of ranked perturbagens/MoAs were shortlisted by removing those with only three counts and P-values more than 0.05, and the top perturbagens/MoAs were selected to experimentally investigate their repurposing performance.

DEGs shared between the five sets and the PKC activator-induced signatures were examined using a Venn diagram generated via the *ggVennDiagram* package[55] and further visualised through an UpSet plot created using the *ComplexHeatmap* package[56]. Comparative GO and pathway enrichment analyses were performed using the

Fig. 5 | Prostratin induces intestinal glucose excretion via aPKC activation in diabetic mice. A Effects of daily i.p. prostratin injection (0.5 mg/kg) on body weight compared with that of saline treatment in db/db mice. **B** Intraperitoneal glucose tolerance tests (GTTs) (Data **A** and **B**, *n* = 6 per group, two-way ANOVA followed by Bonferroni's multiple comparisons test). **C** Area under curve (AUC) comparison of intraperitoneal glucose tolerance tests in db/db mice treated with either vehicle or prostratin (*n* = 6 mice per group). **D** Post-washing FDG autoradiography of vehicle- or prostratin-treated intestinal specimens. **E** FDG biodistribution analysis in prostratin- and vehicle-treated mice revealing higher FDG uptake in the intestine of prostratin-treated mice, *n* = 4 mice per group. **F** Intestinal lumen PBS washing depicting increased FDG excretion in prostratin-treated mice. *n* = 3–4 per group. **G** Representative transmission electron microscopic images of the ileal intestinal brush border membrane and cell junctions of prostratin- and vehicle-treated mice, *n* = 3 per group. Representative images of **H** PKCζ and **I** GLUT1 immunostaining in the jejunum and ileum of prostratin- or vehicle-treated mice. Scale bar = 50 μm, *n* = 3 per group. **J**–**L** db/db mice treated with vehicle or prostratin were placed into metabolic cages for 72 h to measure average: **J** food consumption (**G**), **K** body heat (kcal/h/kg), and **L** activity level (Counts) (Data in **J**–**L**, *n* = 4 mice per group). All data are presented as the mean ± SEM. Data in (**C**, **E**, and **F**) were analysed using two-sided Mann–Whitney *U* test; *$P < 0.05$, **$P < 0.01$, ***$P < 0.001$ vs. Vehicle. Source data are provided as a Source Data file.

Metascape platform[57] under default conditions, with modifications such that only functional sets, pathways (excluding Hallmark Gene Sets), and structural complexes (excluding CORUM) were considered. The top GO and pathway analyses findings were visualised using heatmap plots, while the cellular component category of the GO enrichment was illustrated using bubble plots on the *ggplot2* package.

Animals and diets

OLETF rats, DIO mice, db/db mice, and streptozotocin (STZ)-induced diabetic mice were maintained on either a standard laboratory chow diet or a high-fat diet, as indicated. The standard chow diet (LabDiet, catalogue no.5002) and the high-fat diet (Research Diet, catalogue no. D12492; 60% kcal from fat) were used. For RYGB experiments, animals were fasted post-operatively, provided a liquid diet for 48–72 h, and subsequently returned to their pre-operative diet. DIO mice were maintained on a high-fat diet, whereas db/db and STZ-induced diabetic mice were maintained on standard chow. All diets were provided ad libitum. Mice were housed under specific pathogen-free conditions with a 12 h light/12 h dark cycle, at an ambient temperature of 22 ± 2 °C and relative humidity of 40–60%. All mouse strains used in this study were on a C57BL/6J genetic background. Male mice were used throughout, and the age of animals at the start of each experiment is specified for each experimental model below.

All mice were maintained in accordance with the regulations of the IACUC of Severance Hospital, Seoul, Republic of Korea (2021-0287). To test the effect of aPKC on the intestinal glucose efflux effect, four-week-old male DIO C57BL/6J mice were obtained from Jackson Laboratory (JAX#380050). Upon arrival, the mice were maintained on a high-fat diet for 20 weeks. After an intraperitoneal glucose tolerance test to determine baseline glucose levels, mice were transfected with either control plasmid or aPKC plasmid through tail vein injections.

To overexpress aPKC in IEC, 4-week-old male Villin-Cre mice were maintained on a high-fat diet for 5 weeks. Villin-Cre mice were fasted overnight and injected with 100 μL Cre-dependent AAVs three times, containing the aPKC sequence and GFP protein in the opposite orientation flanked by two inverted loxP sites (AAV-CMV-PKCλ;1.5×10^{14} GC/mL and AAV-CMV-PKCζ), or AAVS, containing only GFP (AAV-CMV-GFP), into tail vein. The mice were allowed to recover and express AAV for 4 weeks before the experiments.

To test the effect of prostratin on the intestinal glucose excretion effect, 5-week-old db/db mice were obtained from Jackson Laboratory (JAX#00064). Mice were intraperitoneally injected with either 0.5 mg/kg prostratin (Sigma Aldrich) once daily or vehicle (saline only) for 4 weeks. Post-treatment, intraperitoneal glucose tolerance tests were performed on the day of sacrifice after overnight fasting. Immediately before sacrifice, blood samples were drawn from the retro-orbital sinus and insulin 1 concentrations were determined by ELISA. The small intestines were removed for autoradiography and further molecular analyses. Streptozotocin injected diabetic mice (STZ-diabetic mice) were established by intraperitoneal injection with STZ (Sigma Aldrich) (75 mg/kg body weight; freshly dissolved in 0.05 M citrate buffer pH, 4.5) for 3 days. These STZ-diabetic mice then injected with prostratin (0.5 mg/kg) or vehicle (saline) for 5 days. Only male mice were used in this study to reduce biological heterogeneity and to ensure experimental consistency. Sex was therefore not considered as a biological variable in the study design or analysis, and no sex-disaggregated analyses were performed.

FRET imaging

Cells expressing aPKC kinase activity reporter were rinsed with Hank's balanced salt solution containing 1 mM $CaCl_2$ and imaged using Zeiss LSM780 microscope (Carl Zeiss). CFP and FRET images were obtained every five seconds using a 420/20-nm excitation filter, a 450-nm dichroic mirror, and a 475/40-nm (CFP) or 535/25-nm (FRET) emission filters. Integration times were 200 ms for CFP and FRET and 100 ms for yellow fluorescent protein. The cellular region with no net movement of the targeted reporter was selected. The trace for each imaged cell was normalised to its $t = 0$ to 6 min averaging baseline value. The normalised C/Y emission ratios calculated from three independent experiments were represented as the average ±SE.

aPKC kinase activity assay

PKCι and PKCζ kinase activity was assessed using a kinase activity kit (Cat. No. ADI-EKS-420A, Enzo Life Sciences, USA), according to manufacturer's protocol. Briefly, 10 ng purified PKCζ or 10 ng purified PKCι was incubated with 10 μM ATP, 0.2 μg/μL substrate, and prostratin at the indicated concentrations (0, 0.5 and 1 μM) for 60 min at 25 °C. After incubation, PKC kinase activity at 450 nm wavelength was detected using the BioTek Synergy HT Multi-Mode Microplate Reader (Agilent Technologies, Inc.). Kinase activity is represented as the relative PKC activity compared to that in the untreated control.

Measurement of cellular glucose uptake

Glucose uptake was quantified by measuring the uptake of 2-DG (Promega Corporation) by cells, according to manufacturer's protocol. Briefly, cells treated with vehicle or drugs were cultured in 96-well plates. They were next incubated in glucose-free media for 30 min. Then, 2-DG (1 mM) was added to the cells and incubated for 15 min. Finally, 2-DG-6-phosphate was detected as a luminescence activity using a 0.3–1 s integration on the Biotek Synergy HT Multi-Mode Microplate Reader (Agilent Technologies, Inc.).

Measurement of glycolysis

Real-time analysis of the ECAR, as a proxy of cellular glycolysis, was performed using the Seahorse XFp Analyzer (Agilent; S7802A). Glycolytic function and capacity were determined with the Seahorse XF Glucose Stress Test Kit (Agilent, 103017-100) according to the manufacturer's protocol. Briefly, cells were subjected to sequential injections of 7.5 mM glucose, 1.0 μM oligomycin (an ATP synthase inhibitor), and 25 mM 2-DG (a glycolysis inhibitor). Upon completion of the assay, ECAR values were normalised to the total protein content in each well, which was quantified using a bicinchoninic acid protein assay. Data were processed and analysed using Seahorse Wave Desktop software (v2.6.0, Agilent).

Intestinal cell glucose secretion

Glucose release from small intestine cells into the culture media was assessed using in vitro permeability assay. Cells were seeded (0.2×10^6) into the 12-well upper insert and incubated at 37 °C in 5% CO_2 atmosphere until a confluent monolayer is formed. Serum deficient, glucose-rich DMEM was added to the culture with prostratin or PBS for 12 h at 37 °C in 5% CO_2 atmosphere. Phenol-free 25 mM glucose and 5 mM FITC-dextran (Sigma Aldrich) containing DMEM medium were added in the upper well. Phenol free no glucose DMEM was added to each well of the receiver well and incubated for 30 min at 37 °C in 5% CO_2 atmosphere. Glucose excretion was then measured in the receiver well with Glucose Colorimetric Detection kit (Thermo Fisher) and normalised to the leakage of FITC-dextran.

Tissue lysate preparation, SDS-PAGE, and western blot analysis

Frozen intestinal tissues, IEC18 cells, or human intestinal organoids were lysed using ice-cold lysis buffer (Cell Signaling Technology, Danvers, MA, USA) containing 1× protease inhibitors (Sigma Aldrich). The samples were homogenised, and protein level in lysates was determined using a Bradford Assay Kit (Bio-Rad Laboratories, Hercules, CA, USA) following the manufacturer's instructions. Equal amounts of protein from each cell lysate were then separated on precast 4–12% NuPAGE Bis-Tris gels (Invitrogen) in a XCell SureLock Mini-Cell (Invitrogen), using 3-(N-morpholino) propanesulfonic acid as the running buffer. Proteins were transferred to polyvinylidene difluoride membranes (Immobilon-P; EMD Millipore, Billerica, MA, USA) at 400 mA and 4 °C for 75 min using a wet transfer system (Bio-Rad Laboratories). Membranes were blocked in 5% milk dissolved in TBS containing 0.05% Tween-20 (TBS-T) for 1 h at ambient temperature. Primary antibodies were diluted in 5% milk or 5% BSA in TBS-T following the manufacturer's recommendations. The following antibodies were used: anti-GLUT-1 (1:5 000; Abcam); anti-Na/K ATPase, anti-GLUT2 (1:3000; Novus, Littleton, CO); anti-PKCα, anti-PKCδ, anti-PKCζ and anti-PKCι (all 1:1 000; Cell Signaling Technology). Blots were incubated overnight with primary antibodies at 4 °C. After washing with TBS-T, the blots were incubated with goat anti-rabbit IgG coupled to HRP (Santa Cruz Biotechnology) or goat anti-mouse IgG HRP (Santa Cruz Biotechnology) in 5% milk dissolved in TBS-T for 1 h 30 min at ambient temperature. The following antibodies were used: anti-GLUT1 (Abcam, ab115730; 1:5000), anti-Na+/K+ ATPase (Abcam, ab76020; 1:10,000), anti-GLUT2 (Novus Biologicals, NBPI-22218; 1:3000), anti-PKCα (Cell Signaling Technology, #59754; 1:1000), anti-PKCδ (Cell Signaling Technology, #2058; 1:1000), anti-PKCζ (Cell Signaling Technology, #9368; 1:1000), and anti-PKCι (Abcam, ab108970; 1:1000). Anti-β-actin antibody (sc-47778, 1:10000; Santa Cruz) and anti-Na/K ATPase (1:10,000; Novus, Littleton, CO) were used as loading control.

ELISA

Mice were fasted for 16 h, and blood samples were drawn from the retro-orbital sinus. Total serum GLP-1 (EGLP-35K, Millipore) and insulin (EZRMI-13K, Millipore) were measured following the manufacturers' instructions. All samples were tested in triplicate.

Small intestinal biodistribution and faecal analyses

After an 8 h fast, approximately 0.2 mCi of FDG was injected intravenously. One hour later, mice were euthanised in a CO_2 chamber while being ventilated with 1% isoflurane in air, and their organs were excised, weighed, and gamma-counted (Wallac Wizard 3" 1480 Gamma Counter; PerkinElmer, Akron, OH, USA). For small intestinal biodistribution and faecal analyses, the intact tract from the stomach to the colon was excised. Post-lavage fluids were flushed using Dulbecco's PBS (DPBS) through the small intestine or colon and harvested for gamma counting, reported as total radioactivity (counts per minute). Finally, FDG distribution in the post-washed small intestine was determined using autoradiography by exposing a phosphorimaging plate (BAS-SR 2040; Fujifilm, Tokyo, Japan) to the small intestine for 10 min. The imaging plate was then scanned using a bio-imaging analyser (FLA7000; Fujifilm). FDG organ biodistribution data were decay-corrected according to the time of anaesthesia and normalised to both the tissue mass (mg) and the radioactivity level upon injection. Final results were expressed as units of ID%/mg. To measure FDG in the small intestinal washes, the counts per minute were normalised to the dose of radioactivity injected, presented in units of ID%.

Crypt isolation and culture for organoid studies

Human small intestine tissues were harvested and transferred into a 15 mL tube containing DPBS.

To eliminate fat, intestines were washed with DPBS using a 10 mL syringe and needle in a 10-cm dish. The intestine was longitudinally cut, and the villi were scraped off using a coverslip. The intestine was then cut into small pieces and transferred into a 50-mL tube in pre-chilled DPBS; the residual villi were removed by vigorous shaking. Pieces of intestinal tissue were transferred into another 50 mL tube with pre-chilled DPBS, and the supernatant was removed. This step was repeated until the supernatant became clear. The intestinal tissues were transferred to a 15-mL tube containing 10 mL of Gentle Cell Dissociation Reagent (#07174; STEMCELL Technologies) and incubated at ambient temperature for 15 min to isolate crypts. After incubation, the crypt suspension was passed through a 70 µm cell strainer into a 50 mL tube containing 30 mL DPBS and centrifuged at 400 × *g* for 3 min. After eliminating the supernatant, 50–200 crypts were suspended in 25 µL of Matrigel® (#356231; BD). The crypt-Matrigel suspension was seeded in the centre of each well of a pre-warmed 48-well plate, which was then incubated at 37 °C for 10 min to solidify the Matrigel. IntestiCult™ growth medium (#06010, 250 µL; STEMCELL Technologies) was added and changed every two to three days.

GLUT1 surface staining

To examine surface GLUT1 expression, IEC6 and IEC18 cells were incubated either with prostratin or DPBS for 1 h. They were then resuspended (10^7/mL) and stained with GLUT1 antibody (1:50; ab115730, Abcam) in 100 µL of flow cytometry buffer made of DPBS containing 1% foetal bovine serum (FACS buffer) at 4 °C for 1 h. The cells were washed with ice-cold FACS buffer for three times and stained with PE-conjugated secondary donkey anti- rabbit (1: 100; ab7008, Abcam) in 100 µL FACS buffer at 4 °C for 1 h. After staining, cells were washed and re-suspended using FACS buffer at 4 °C. Cells were analysed using a FACSVERSE instrument (BD Biosciences, San Jose, CA, USA) and FlowJo (BD Biosciences).

Statistics and reproducibility

All data are presented as mean ± SEM with the number of experiments or mice indicated in the figure legends. Unpaired Student's *t*-test or Mann–Whitney *U* test was employed for comparisons between two groups, One-way analysis of variance with Fisher's LSD post-hoc test or Kruskal–Wallis test with Dunn's post-hoc test was used for multiple group comparisons, and two-way ANOVA with Dunnett's multiple comparisons test was used to determine the statistical significance. The significance levels are $^{***}P < 0.001$; $^{**}P < 0.01$; $^{*}P < 0.05$. For all analyses, $P < 0.05$ was considered statistically significant. Statistical analyses were performed using GraphPad Prism 9.0 (GraphPad Software, San Diego, CA, USA). The specific statistical test used and the number of experiments performed for each analysis are indicated in the corresponding figure legend. Normal distribution was assumed for all analyses, and no data points were excluded. All experiments were performed three or more times independently under identical or similar conditions.

Reporting summary

Further information on research design is available in the Nature Portfolio Reporting Summary linked to this article.

Data availability

The RNA sequencing data generated in this study have been deposited in the NCBI Gene Expression Omnibus under accession numbers GSE239399 [https://www.ncbi.nlm.nih.gov/geo/query/acc.cgi?acc=GSE239399] and GSE240754 [https://www.ncbi.nlm.nih.gov/geo/query/acc.cgi?acc=GSE240754]. The single-cell RNA sequencing data used in this study are available in GEO with the accession number GSE312264 [https://www.ncbi.nlm.nih.gov/geo/query/acc.cgi?acc=GSE312264]. Source Data are provided with this paper. Any additional information required to reanalyse the data reported in this study is available from the corresponding author upon reasonable request. Detailed information on differentially expressed genes (DEGs) from the RNA-seq and REMEDY datasets is included in the Source Data file. Source data are provided with this paper.

References

1. Pories, W. J., Flickinger, C. aroJ. F., Meelheim, E. G. & Swanson, H. D. MS. The control of diabetes mellitus (NIDDM) in the morbidly obese with the Greenville Gastric Bypass. *Ann. Surg.* **206**, 316–323 (1987).
2. Pories, W. J. et al. Is type II diabetes mellitus (NIDDM) a surgical disease? *Ann. Surg.* **215**, 633–642 (1992).
3. Schauer, P. R. et al. Bariatric surgery versus intensive medical therapy for diabetes-3-year outcomes. *N. Engl. J. Med.* **370**, 2002–2013 (2014).
4. Pories, W. J. et al. Who would have thought it? An operation proves to be the most effective therapy for adult-onset diabetes mellitus. *Ann. Surg.* **222**, 339–350 (1995).
5. Kwon, I. G. et al. Serum glucose excretion after Roux-en-Y gastric bypass: a potential target for diabetes treatment. *Gut* **70**, 1847–1856 (2021).
6. Ku, C. R. et al. Intestinal glycolysis visualized by FDG PET/CT correlates with glucose decrement after gastrectomy. *Diabetes* **66**, 385–391 (2017).
7. Oh, J. H. et al. Altered glucose metabolism and glucose transporters in systemic organs after bariatric surgery. *Front. Endocrinol.* **13**, 937394 (2022).
8. Cavin, J. B. et al. Differences in alimentary glucose absorption and intestinal disposal of blood glucose after Roux-en-Y gastric bypass vs sleeve gastrectomy. *Gastroenterology* **150**, 454–464.e459 (2016).
9. Jurowich, C. F. et al. Duodenal-jejunal bypass improves glycemia and decreases SGLT1-mediated glucose absorption in rats with streptozotocin-induced type 2 diabetes. *Ann. Surg.* **258**, 89–97 (2013).
10. Troy, S. et al. Intestinal gluconeogenesis is a key factor for early metabolic changes after gastric bypass but not after gastric lap-band in mice. *Cell Metab.* **8**, 201–211 (2008).
11. Saeidi, N. et al. Reprogramming of intestinal glucose metabolism and glycemic control in rats after gastric bypass. *Science* **341**, 406–410 (2013).
12. Ekins, S., Mestres, J. & Testa, B. In silico pharmacology for drug discovery: applications to targets and beyond. *Br. J. Pharm.* **152**, 21–37 (2007).
13. Kharkar, P. S., Warrier, S. & Gaud, R. S. Reverse docking: a powerful tool for drug repositioning and drug rescue. *Future Med. Chem.* **6**, 333–342 (2014).
14. Pushpakom, S. et al. Drug repurposing: progress, challenges and recommendations. *Nat. Rev. Drug Discov.* **18**, 41–58 (2019).
15. Subramanian, A. et al. A next generation connectivity map: L1000 platform and the first 1,000,000. *Profiles Cell* **171**, 1437–1452.e1417 (2017).
16. Lamb, J. et al. The connectivity map: using gene-expression signatures to connect small molecules, genes, and disease. *Science* **313**, 1929–1935 (2006).
17. Duan, Q. et al. L1000CDS(2): LINCS L1000 characteristic direction signatures search engine. *NPJ Syst. Biol. Appl.* **2**, 16015 (2016).
18. Musa, A. et al. A review of connectivity map and computational approaches in pharmacogenomics. *Brief. Bioinform.* **19**, 506–523 (2018).
19. Siller, G., Gebauer, K., Welburn, P., Katsamas, J. & Ogbourne, S. M. PEP005 (ingenol mebutate) gel, a novel agent for the treatment of actinic keratosis: results of a randomized, double-blind, vehicle-controlled, multicentre, phase IIa study. *Australas. J. Dermatol.* **50**, 16–22 (2009).
20. Ersvaer, E. et al. The protein kinase C agonist PEP005 (ingenol 3-angelate) in the treatment of human cancer: a balance between efficacy and toxicity. *Toxins* **2**, 174–194 (2010).
21. Szallasi, Z., Krsmanovic, L. & Blumberg, P. M. Nonpromoting 12-deoxyphorbol 13-esters inhibit phorbol 12-myristate 13-acetate induced tumor promotion in CD-1 mouse skin. *Cancer Res.* **53**, 2507–2512 (1993).
22. Zayed, S., Sorg, B. & Hecker, E. Structure activity relations of polyfunctional diterpenes of the tigliane type, VI. Irritant and tumor promoting activities of semisynthetic mono and diesters of 12-deoxyphorbol. *Planta Med.* **50**, 65–69 (1984).
23. Griner, E. M. & Kazanietz, M. G. Protein kinase C and other diacylglycerol effectors in cancer. *Nat. Rev. Cancer* **7**, 281–294 (2007).
24. Newton, A. C. & Brognard, J. Reversing the paradigm: protein kinase C as a tumor suppressor. *Trends Pharm. Sci.* **38**, 438–447 (2017).
25. Ono, Y. et al. Nucleotide-sequences of cDNAs for alpha-subspecies and gamma-subspecies of rat-brain protein kinase-C. *Nucleic Acids Res.* **16**, 5199–5200 (1988).
26. Ono, Y. et al. The structure, expression, and properties of additional members of the protein kinase-C family. *J. Biol. Chem.* **263**, 6927–6932 (1988).
27. Kanoh, Y. et al. Defective activation of atypical protein kinase C zeta and lambda by insulin and phosphatidylinositol-3,4,5-(PO4)(3) in skeletal muscle of rats following high-fat feeding and streptozotocin-induced diabetes. *Endocrinology* **144**, 947–954 (2003).
28. Farese, R. V. et al. Muscle-specific knockout of PKC-lambda impairs glucose transport and induces metabolic and diabetic syndromes. *J. Clin. Invest.* **117**, 2289–2301 (2007).
29. Yu, H. et al. Contraction stimulates muscle glucose uptake independent of atypical PKC. *Physiol. Rep.* **3**, e12565 (2015).
30. Bailey, M. J. & Prehoda, K. E. Establishment of par-polarized cortical domains via phosphoregulated membrane motifs. *Dev. Cell* **35**, 199–210 (2015).
31. Xu, C. et al. The septate junction protein Tsp2A restricts intestinal stem cell activity via endocytic regulation of aPKC and hippo signaling. *Cell Rep.* **26**, 670–688.e676 (2019).
32. Kajimoto, T. et al. Activation of atypical protein kinase C by sphingosine 1-phosphate revealed by an aPKC-specific activity reporter. *Sci. Signal* **12**, eaat6662 (2019).
33. Beeson, M. et al. Activation of uptake in IEC18 cells treated with DMSO, Pro, or Pro-zeta by insulin and phosphatidylinositol-3,4,5-(PO4)3 is defective in muscle in type 2 diabetes and impaired glucose tolerance: amelioration by rosiglitazone and exercise. *Diabetes* **52**, 1926–1934 (2003).
34. Lee, A. et al. Amino acid-based compound activates atypical PKC and leptin receptor pathways to improve glycemia and anxiety like behavior in diabetic mice. *Biomaterials* **239**, 119839 (2020).
35. Beeson, M. et al. Defective activation of protein kinase C-z in muscle by insulin and phosphatidylinositol-3,4,5,-(PO(4))(3) in obesity and polycystic ovary syndrome. *Metab. Syndr. Relat. Disord.* **2**, 49–56 (2004).

36. Sirota, M. et al. Discovery and preclinical validation of drug indications using compendia of public gene expression data. *Sci. Transl. Med.* **3**, 96ra77 (2011).
37. Kunkel, S. D. et al. mRNA expression signatures of human skeletal muscle atrophy identify a natural compound that increases muscle mass. *Cell Metab.* **13**, 627–638 (2011).
38. Hassane, D. C. et al. Discovery of agents that eradicate leukemia stem cells using an in silico screen of public gene expression data. *Blood* **111**, 5654–5662 (2008).
39. Gao, L. et al. Discovery of the neuroprotective effects of alvespimycin by computational prioritization of potential anti-Parkinson agents. *FEBS J.* **281**, 1110–1122 (2014).
40. Beguinot, F. & Formisano, P. Atypical protein kinase C dysfunction and the metabolic syndrome. *Trends Endocrinol. Metab.* **19**, 39–41 (2008).
41. Schmitz-Peiffer, C. & Biden, T. J. Protein kinase C function in muscle, liver, and beta-cells and its therapeutic implications for type 2 diabetes. *Diabetes* **57**, 1774–1783 (2008).
42. Bosch, R. R. et al. Regulation of GLUT1-mediated glucose uptake by PKClambda-PKCbeta(II) interactions in 3T3-L1 adipocytes. *Biochem. J.* **384**, 349–355 (2004).
43. Tobar, N. et al. Metformin acts in the gut and induces gut-liver crosstalk. *Proc. Natl. Acad. Sci. USA* **120**, e2211933120 (2023).
44. Duca, F. A. et al. Metformin activates a duodenal Ampk-dependent pathway to lower hepatic glucose production in rats. *Nat. Med.* **21**, 506–511 (2015).
45. McCreight, L. J., Bailey, C. J. & Pearson, E. R. Metformin and the gastrointestinal tract. *Diabetologia* **59**, 426–435 (2016).
46. Tsuchida, H., Morita, Y., Nogami, M. & Ogawa, W. Metformin action in the gut-insight provided by [(18)F]FDG PET imaging. *Diabetol. Int.* **13**, 35–40 (2022).
47. Morita, Y. et al. Enhanced release of glucose into the intraluminal space of the intestine associated with metformin treatment as revealed by [(18)F]Fluorodeoxyglucose PET-MRI. *Diab. Care* **43**, 1796–1802 (2020).
48. Sakaguchi, K. et al. Metformin-regulated glucose flux from the circulation to the intestinal lumen. *Commun. Med.* **5**, 44 (2025).
49. Kudo, Y. et al. PKClambda/iota loss induces autophagy, oxidative phosphorylation, and NRF2 to promote liver cancer progression. *Cancer Cell* **38**, 247–262.e211 (2020).
50. Wang, M. T. et al. K-Ras promotes tumorigenicity through suppression of non-canonical Wnt signaling. *Cell* **163**, 1237–1251 (2015).
51. Blandino, G. et al. Metformin elicits anticancer effects through the sequential modulation of DICER and c-MYC. *Nat. Commun.* **3**, 865 (2012).
52. Xie, J. et al. GPD1 enhances the anticancer effects of metformin by synergistically increasing total cellular glycerol-3-phosphate. *Cancer Res.* **80**, 2150–2162 (2020).
53. Williams, S. A. et al. Prostratin antagonizes HIV latency by activating NF-kappaB. *J. Biol. Chem.* **279**, 42008–42017 (2004).
54. Muller, T. D. et al. Glucagon-like peptide 1 (GLP-1). *Mol. Metab.* **30**, 72–130 (2019).
55. Gao, C. H., Yu, G. & Cai, P. ggVennDiagram: an intuitive, easy-to-use, and highly customizable R package to generate venn diagram. *Front. Genet.* **12**, 706907 (2021).
56. Gu, Z., Eils, R. & Schlesner, M. Complex heatmaps reveal patterns and correlations in multidimensional genomic data. *Bioinformatics* **32**, 2847–2849 (2016).
57. Zhou, Y. et al. Metascape provides a biologist-oriented resource for the analysis of systems-level datasets. *Nat. Commun.* **10**, 1523 (2019).

Acknowledgements

This research was supported by a grant from the Korea Health Technology R&D Project through the Korea Health Industry Development Institute (KHIDI), funded by the Ministry of Health & Welfare and the Republic of Korea [grant number: RS-202400437692 to Cheol Ryong Ku (CRK)] and the Bio & Medical Technology Development Program of the National Research Foundation (NRF) funded by the Korean government (MSIT) (No. NRF-2022M3E5F3081268). We appreciate the Medical Illustration & Design (MID) team, a member of Medical Research Support Services of Yonsei University College of Medicine, for their excellent support with the medical illustrations.

Author contributions

Conceptualisation: C.R.K. Methodology: M.E.F., U.K., S.S.H., H.H.K., J.P., J.S.K. Investigation: C.W.K., Z.H., J.H.O., E.K.W., S.L., J.H.N., H.S., Y.B.K., Y.J.L., H.J., J.W.J., D.K. Visualisation: C.W.K., Z.H. Funding acquisition: C.R.K. Project administration: C.R.K. Supervision: C.R.K., I.S., S.F., B.K.L. Writing–original draft: C.W.K., Z.H., C.R.K. Writing–review & editing: C.R.K., J.P., H.J.C., E.J.L., A.C., Y.J.L.

Competing interests

C.W.K., J.H.O., E.K.W. and C.R.K. are co-inventors on a pending patent application (PCT/KR2022/002035) filed by Yonsei University College of Medicine and Arontier Corporation, covering a composition for glucose regulation containing aPKC activators described in this manuscript. I.S., Z.H, M.E.F. and U.K. are employees of Arontier Corporation. The remaining authors declare no competing interests.

Additional information

Supplementary information The online version contains supplementary material available at https://doi.org/10.1038/s41467-026-69193-7.

Correspondence and requests for materials should be addressed to Cheol Ryong Ku.

Peer review information *Nature Communications* thanks Hannah Gilliam-Vigh and Xun Lan, and the other, anonymous, reviewer(s) for their contribution to the peer review of this work. A peer review file is available.